Title

First Principles Study of Aluminum Doped Polycrystalline Silicon as a Potential Anode Candidate in Li-ion Batteries

Permalink

https://escholarship.org/uc/item/84d5m6cr

Authors

Bhimineni, Sree Harsha

Ko, Shu-Ting

Xia, Yantao

et al.

Publication Date

2024-03-19

DOI

10.26434/chemrxiv-2024-qpdp3

Supplemental Material

https://escholarship.org/uc/item/84d5m6cr#supplemental

First Principles Study of Aluminum Doped Polycrystalline Silicon as a Potential Anode Candidate in Li-ion Batteries

Sree Harsha Bhimineni,[†] Shu-Ting Ko,[‡] Casey Cornwell,[¶] Yantao Xia,[†] Sarah H. Tolbert,[¶,§] Jian Luo,[‡,∥] and Philippe Sautet[*,†,¶]

†Department of Chemical and Biomolecular Engineering, University of California, Los Angeles, California, 90095

‡Program in Materials Science and Engineering, University of California San Diego, La Jolla, California, 92093

¶Department of Chemistry and Biochemistry, University of California, Los Angeles, California, 90095

§Department of Materials Science and Engineering, University of California, Los Angeles, California, 90095

∥Aiiso Yufeng Li Family Department of Chemical and Nano Engineering, University of California San Diego, La Jolla, California, 92093

E-mail: sautet@ucla.edu

Abstract

Addressing sustainable energy storage remains crucial for transitioning to renewable sources. While Li-ion batteries have made significant contributions, enhancing their capacity through alternative materials remains a key challenge. Micro-sized silicon is a promising anode material due to its tenfold higher theoretical capacity compared to conventional graphite. However, its substantial volumetric expansion during cycling impedes practical application due to mechanical failure and rapid capacity fading. We propose a novel approach to mitigate this issue by incorporating trace amounts of aluminum into the micro-sized silicon electrode using ball milling. We employ density functional theory (DFT) to establish a theoretical framework elucidating how grain boundary sliding, a key mechanism involved in preventing mechanical failure, is facilitated by the presence of trace aluminum at grain boundaries. This, in turn, reduces stress accumulation within the material, reducing the likelihood of failure. To validate our theoretical predictions, we conducted capacity retention experiments on undoped and Al-doped micro-sized silicon samples. The results demonstrate significantly reduced capacity fading in the doped sample, corroborating the theoretical framework and showcasing the potential of aluminum doping for improved Li-ion battery performance.

Introduction

Lithium-ion batteries have become a norm for energy storage these days. Many advances to increase their efficiency have been proposed. In the realm of material science, electrode, electrolyte, and separator are interesting design elements. Specifically focusing on anodes, several materials are being explored such as graphitic materials, metals, metal oxides, and metal phosphide.[1] A key material explored is silicon. The obvious reason for silicon being a promising candidate is its high theoretical specific capacity (4200 mA-h/g for $Li_{22}Si_5$[2]) compared to the current graphite anode (372 mA-h/g[3]). Furthermore, silicon is the second-most abundant element in the earth's crust, making it a readily available material. However, its practical implementation is limited by a main bottleneck, the huge volumetric expansion after lithiation (310% for $Li_{22}Si_5$[4]) which causes a large build-up of stress, resulting in the pulverization of the material and immediate capacity loss during cycling.[5–9] An example is the loss of 70% of the capacity of silicon anode made from 10 μm silicon powder within the first five cycles.[10] There has been a surge in research output to tackle this bottleneck over the past decade.[11] Specifically, one focus of research is on using micro-nano sized particle silicon anodes as they have been shown to resist cracking and accommodate the volumetric change.[11–13] However, the improvement is still not sufficient for practical application. Other cutting edge research concentrates on modifying the anode by the formation of alloys,[14–16] composites,[17–19] core-shell structures,[20,21] films[22,23] and porous systems.[24,25]

On the fundamental aspect, unavoidable volume expansion in each crystalline grain of silicon upon lithiation creates important mechanical stress in the material, responsible for rupture. A major mechanism to relieve this stress would be to allow facile sliding at the grain boundaries.[26,27] Previous experimental observations of GB sliding have been predominantly limited to metallic materials such as Al, Cu, Sn, Zn, and Mg.[28–32] To our knowledge, there has been no work in the literature for GB sliding in silicon. This comes from the fact that silicon has strong covalent bonds, which may render GB sliding highly activated and inoperative at near ambient temperature. In this manuscript, we study GB sliding in silicon

using first-principle atomistic simulations. We show that GB sliding in silicon is activated and that doping silicon with aluminum markedly facilitates GB sliding, and is, therefore, a potential solution to improve the mechanical properties and durability of silicon anodes upon cycling. We show that the small amount of aluminum segregates in the grain boundaries (GBs) of silicon and greatly facilitates GB sliding. The prevalence of the $\Sigma 3$ {111} GB in polycrystalline materials has been well-documented in numerous previous studies[33–35] and is revealed in our GB characteristics quantification by electron backscattered diffraction (Supporting Information Figure S1). Recognizing its significance, we have consistently employed the $\Sigma 3$ {111} GB in all our simulations. We have devised a unique model to perform grain boundary sliding simulations. Our investigative approach encompasses the utilization of basin hopping, a global optimization technique to understand the segregation of aluminum in the GB. Through this computational framework, we seek to gain insights into the influence of aluminum on GB sliding behavior, hence enabling the reorganization of the polycrystalline silicon anode without mechanical failure during lithiation. To validate the simulation results, micro-sized polycrystalline silicon powders are experimentally doped with 5 wt.% (4.9 mol.%) aluminum and mixed by high-energy ball milling. Using our charge-discharge cycling test of half cells, we show that aluminum-doped silicon anode exhibits improved capacity retention than the undoped counterpart. We believe that this is an innovative and cost-effective way of improving the cyclic stability of silicon anodes.

Methods

Energy Calculations

All electronic energy calculations are performed with Density Functional Theory (DFT), implemented using the Vienna ab initio simulation package (VASP).[36] The atomic simulation environment (ASE)[37] is used in conjunction with VASP to develop our custom automation scripts in Python which are available at GitHub.[38] The electron-ion interactions are treated

4

using the projected augmented wave (PAW) method. The exchange-correlation effects are incorporated using the Perdew-Burke-Ernzerhof (PBE) functional.[39] The Brillouin-zone integration is performed using Monkhorst pack[40] k-point grids of 15x9x1 for all the calculations. To improve the convergence of the calculation with respect to the k-points, tetrahedron smearing with Blöchl corrections is used. The valence electrons are considered as a set of plane waves according to the Bloch theorem with a cutoff energy of 300 eV. All the structures are geometrically optimized using the conjugate gradient algorithm until the force on each atom is less than 0.01 eV/Å.

Generation of $\Sigma 3$ Grain Boundary

The $\Sigma 3$ (GB) can be described as a twist boundary characterized by a layered structure. In this GB, each grain's top and bottom layers are derived from bulk silicon with a relative twist angle of 60° between them. We have implemented the bicrystal model of GB. Subsequently, layers from each grain are systematically stacked atop one another, a process facilitated by our custom Python script.[38] One notable advantage of this approach is the precise control it provides over the number of layers within each grain, allowing for tailored investigations. The GB is characterized by its interface energy which is defined according to Equation 1.

$$E_{GB}^I = \frac{E_{GB} - n_{Si}E_{BulkSi} - n_{Al}E_{BulkAl}}{2A} \tag{1}$$

where E_{GB}^I is the interface energy of the GB, E_{GB} is the energy of the GB supercell, n_{Si} is the number of silicon atoms in the GB, E_{BulkSi} is the per atom energy of bulk diamond cubic silicon, n_{Al} is the number of aluminum atoms in the GB, E_{BulkAl} is the per atom energy of bulk fcc aluminum and A is the interface area of the GB. The factor 2 is incorporated to indicate the presence of two GBs in the unit cell.
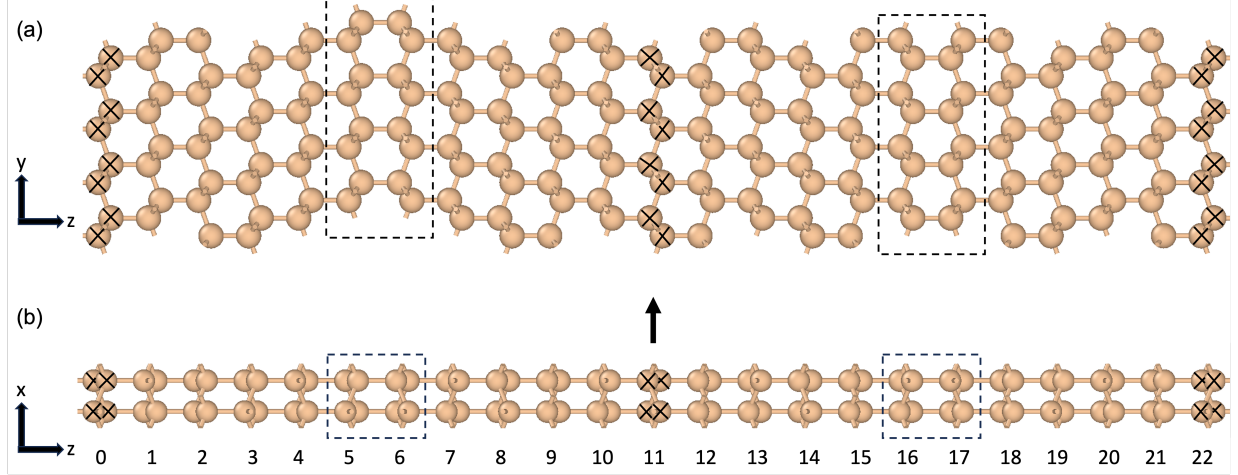
Figure 1: Schematic diagram of $\Sigma3\{111\}$ GB orthorhombic supercell including 11 layers per grain. (a) View perpendicular to the yz plane showing the periodicity in the y direction, the cell has been doubled in the y direction (with respect to the cell used in the calculations) for clarity; and (b) View perpendicular to the xz plane. The dashed boxes indicate GBs, cross marks indicate the atoms that are fixed to model the sliding process, the arrow indicates the direction of sliding and the numbers indicate the layer index.

Aluminum Segregation Exploration

In order to obtain the most stable configuration for the aluminum segregation in the GB, we use the Basin Hopping algorithm which is based on the canonical Monte Carlo technique,[41] where the algorithm alters the coordinates of the current structure to a new structure according to a predefined constraint and then geometrically optimizes it. The optimized new structure can be accepted or rejected based on the Metropolis criterion.[42] The results are interpreted using aluminum substitution energy as defined in Equation 2. The decision to employ the basin-hopping technique in our research is inspired by the work of Sun *et al.* In their study, Sun *et al.* successfully applied this method to investigate the behavior of a Pt_8 cluster on an alumina substrate under varying hydrogen pressures.[43]

$$E_{Al} = E_{GB+nAl} - E_{GB} - n_{Al}E_{BulkAl} + n_{Al}E_{BulkSi} \tag{2}$$

where E_{Al} is the aluminum substitution energy, E_{GB+nAl} is the energy of the grain boundary

6

with substituted aluminum, n_{Al} is the number of substituted aluminum, E_{GB} is the energy of the GB without aluminum, E_{BulkAl} is the per atom energy of bulk fcc aluminum and E_{BulkSi} is the energy per atom of bulk diamond silicon.

Grain Boundary Sliding

The dominant phenomenon observed during mechanical operations at grain boundaries is known as GB sliding. To gain insights into how the segregation of aluminum at GB influences this phenomenon, a comprehensive study of GB sliding becomes imperative. As a result, we have developed a model through our custom Python script.[38] In our approach, we have fixed one layer within each of the grains as shown in Figure 1, preventing any atomic position relaxation. Employing a systematic, serial methodology, we introduce relative displacements between the layers of one grain to the other. Subsequently, the resulting atomic structure is subjected to geometric optimization. These fixed layers effectively serve as constraints, maintaining the deformation within the GB region.

Materials Synthesis and Electrochemical Testing

The micro-sized Si powder (99.995%, 5 um, US-Nano) is mixed with 5 wt.% Al (325 mesh, Alfa Aesar) sealed in hardened steel jars with hardened steel balls under argon. The powder mixture is ball-milled using SPEX 8000 high-energy ball mill for 20 h (1 h milling with 30 min resting interval, 20 cycles). The as-milled powders are meshed using 325 mesh sieve to remove large agglomerates. The undoped Si powders are ball-milled and prepared in the same procedure. To conduct the electrochemical testing on as-prepared powder samples, the active materials are mixed with carbon fiber and carboxymethyl cellulose (CMC) binder in a weight ratio of 70:15:15 with citric acid/KOH aqueous buffer solution (PH=3) as the solvent. The slurry is cast on the copper foils with a following 12h drying in a vacuum oven at 80°C. The electrodes are punched into discs with a mass loading of 0.5 mg/cm^2 for coin cell assembly. The half cells are assembled with Li metals as the counter electrodes, Celgard

7

3501 as separators, and 1M LiPF$_6$ in EC/DEC (1:1 by vol.) with 10 wt.% FEC as the liquid electrolyte. The constant current charge-discharge tests are performed at 0.1C (420 mA/g) with a cut-off voltage of 0.01V and 1.0V.

Electron Microscopy Characterization

The morphology and elemental distribution are observed using a scanning electron microscope (Thermo Scientific Apreo SEM) with energy-dispersive X-ray spectroscopy (Oxford Instruments X-Max 80 EDS detector). The powder samples are mounted in the epoxy and polished to reveal the cross sections for electron back-scattered diffraction (EBSD). Then, EBSD is acquired with Oxford Instruments Symmetry EBSD detector on SEM at 10-15 kV and 13-26 nA. The grain size and GB characteristics are analyzed through HKL Channel 5 (Oxford Instruments) with 920 grains.

The lamella sample for transmission electron microscopy (TEM) was prepared using the focus ion beam on a FEI Quanta 3D FEG Dual Beam Electron Microscope. The nanocrystallites imaging and electron diffraction of Al-doped Si were conducted using Talos F200X G2 TEM at 200kV in TEM bright-field and diffraction mode.

Surface Analysis

X-ray Photoelectron Spectroscopy (XPS) was used for elemental characterization and quantification of material surfaces. Experiments were performed on a Kratos Axis Ultra DLD Spectrometer and photoelectrons were excited using a monochromatic Al Kα radiation source. Photoelectrons were collected with a 20 eV pass energy and 0.1 eV step size, while charging of the sample was controlled using the charge neutralizer filament. Binding energies were calibrated using the adventitious C 1s peak at 284.6 eV, and high-resolution spectra were fit using CasaXPS software. The background was defined using a Shirley line shape, and peak integration with atomic sensitivity factors from the Kratos library were used to quantify elemental ratios in the samples.

Results and Discussions

The calculated lattice parameter of bulk silicon is $a = b = c = 5.43$ Å, which is in agreement with the experimental value of 5.431 Å at 298.5 K[44]. In all our simulations, we examined an 11-layered (11 layers per grain) Σ3 {111} grain boundary (GB) structure with orthorhombic unit cell as described in Section II, with $a = 3.866$ Å, $b = 6.697$ Å and $c = 69.454$ Å as the relaxed lattice parameters, characterized by an interface energy of 1.5 meV/Å^2 agreeing with experimental observations documented in the literature.[45]

Our investigation first aimed at understanding the underlying principles governing aluminum segregation within this system. An important observation is that aluminum exhibits a significant preference for the substitutional site (0.99 eV) over the interstitial site (2.77 eV) in bulk silicon. Furthermore, our findings indicate that it is energetically more favorable for aluminum to occupy the grain boundary substitutional site (0.9 eV) compared to the bulk site (0.99 eV).

Although the preferred position of the Al atom in Si is at the grain boundary, the substitution energy, referenced to bulk Al, is positive, a prediction aligned with the phase diagram.[46] This questions the possibility to reach this metastable state, where Al is dispersed in Si instead of being in the form of bulk Al particles, in the ball milled samples. Experimental characterization by SEM-EDS mapping (Supporting Information Figure S2) shows that the distribution of Si and Al elements in the as-prepared sample are homogeneous with only a trace amount of oxygen, which co-exists with aluminum. By comparison, the oxygen tends to enrich at surfaces, shown by X-ray photon spectroscopy results in Supporting Information Figure S3, which indicates the possibility of oxygen enrichment at GBs. XPS quantification result shows 49.1% Si, 5.9% Al, and 45% O at surfaces (Al/Si =0.12), which is higher than the nominal ratio (Al/Si = 0.049 for 4.9 mol% of Al doping). This further suggests that oxygen can facilitate Al enrichment at surfaces or interfaces.

This is in turn supported by our simulations of systems containing aluminum and oxygen at the GB as shown in Figure 2. The reference for oxygen for calculating aluminum

substitution energy is oxygen in the interstice position of bulk and/or GB for pure Si (-0.09 eV compared to bulk) according to the oxygen's position. Calculations clearly show that the presence of oxygen atoms in Si markedly stabilizes the substitution of Al, and especially at the GB. Al substitution becomes exothermic for 3 O per Al. Small amount of oxygen can hence favor the dispersion of Al in Si, with an optimal placement at GB. This dispersion of Al is additionally facilitated by the high temperature and the large amount of induced defects and grain boundaries during the ball milling synthesis.[47] Although oxygen is present at the surfaces and interfaces of the as-prepared electrode material, this will not be the case for the electrode in the working battery. Indeed, during the first cycle, the highly reducing potential will reduce the oxide to pure metal and Li_2O, leaving metallic Al at grain boundaries throughout the material in a metastable situation. This is supported by galvanostatic cycling tests of the Al-doped Si sample shown in Supporting Information Figure S4, where we compared the specific capacity in the first and second discharge curves above 0.5 V, where the lithiation of crystalline Si has not occurred (the lithiation voltage plateau is around 0.1 V).[48] In the first discharge curve from OCV to 0.5 V, the oxide is reduced and is not reformed due to the upper cutoff potential of 1.0 V. The specific capacity difference between OCV to 0.5 V in the first discharge curve and 0.88 V to 0.5 V in the second discharge curve is 24.52 mAh/g, which suggests that the trace oxide is reduced in the first cycle. Furthermore, below 0.5 V where lithium intercalation occurs, it has been previously observed that the oxygen preferentially interacts with the intercalated lithium to form Li_2O during the cycling of the battery, therefore removing the eventually remaining oxygen atoms.[49] We have attempted a direct determination of Al position with microscopy. Transmission electron microscopy (TEM) has been conducted to investigate the GBs of the Al-doped Si sample. We found that the micro-sized secondary particles (Supporting Information Figure S1) consist of nano-sized crystallites and their nanograin structures impose challenges on GB investigation (Supporting Information Figure S5). Due to the limitation, our TEM experiment cannot conclusively support the results obtained from SEM, XPS and
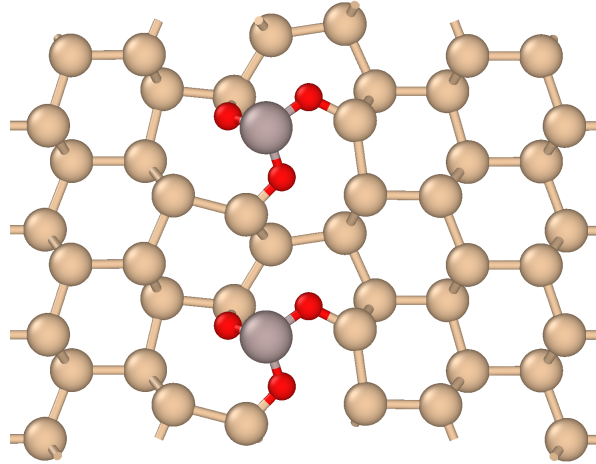
theory.

Figure 2: Schematic of substituted aluminum bonding with three surrounding interstice oxygen atoms in which two are bulk oxygen atoms and one is a GB oxygen atom. The oxygen atoms occupy bridging positions between aluminum and neighboring silicon atoms.

Table 1: Aluminum substitution energy of aluminum substituted GB for different numbers of surrounding oxygen atoms.

Number of oxygen atoms	Aluminum substitution energy in GB (eV)	Aluminum substitution energy in bulk (eV)	Difference between Aluminum substitution energy in bulk and GB (eV)
0	0.9	0.99	0.09
1	0.77	0.92	0.15
2	0.20	0.42	0.22
3	-0.27	-0.08	0.19
4	-0.82	-0.67	0.15

Validation and Characteristics of the GB Sliding Model

Using the algorithm detailed in Section II, we conducted simulations to investigate GB sliding initially using the model of Figure 1 where the GBs are separated by 11 silicon layers as shown in Figure 3. The simulation spanned 20 steps, with each step corresponding to a relative displacement of 0.773 Å (equivalent to one-fifth of the unit cell length in the x-direction, measuring 3.866 Å). Figure 4a illustrates the initial steps characterized by elastic

deformation, where no significant bond restructuring occurs, signifying the absence of sliding. This elastic deformation accumulates stress within the structure, eventually leading to stress release through a sliding event between the relative displacement of 8.506 Å and 9.279 Å (steps 11 and 12 respectively). Notably, this sliding occurs between layers 5 and 6 as can be seen in Figure 4b, as well as 17 and 18, which are the grain boundary layers, as depicted in Figure 1 and 3. Our observation is documented in several previous studies on other materials and has been termed as a saw-tooth mechanism or stick-slip mechanism.[50,51] This validates the accuracy of our model in reflecting GB sliding behavior.

In this context, we define the barrier for GB sliding (ΔE), as expressed in Equation 3.

$$\Delta E = E[max] - E[min] \tag{3}$$

Here, $E[min]$ corresponds to the interface energy of the GB without deformation, while $E[max]$ corresponds to the maximum interface energy of the GB along the deformation. To obtain an accurate value of ΔE, we performed ten GB sliding simulations (with a smaller step corresponding to a displacement of 0.077 Å) between the relative displacement of 8.506 Å and 9.279 Å as shown in Figure 4c. A lower barrier indicates greater ease of sliding and more effective stress release. However, in our current case, the sliding barrier measures 0.33 eV/Å², which is 220 times that of the interface energy of the undeformed GB. This implies a high degree of rigidity in sliding and a consequently elevated risk of structural cracking. Apart from the energetics, since the atoms in layers 0, 11, and 21 are fixed as shown in Figure 1 and 3, they experience a non-zero force when the GB is deformed. The average magnitude of force on the fixed atoms is represented in Figure 4d. This force drops at a relative displacement of 9.279 Å which coincides with the GB sliding. However, the structure and its energy does not return to that of the undeformed state as can be seen in Figure 4a and 4c. Sliding stops at a partially deformed structure, indicating that the stress release is not effective during sliding.
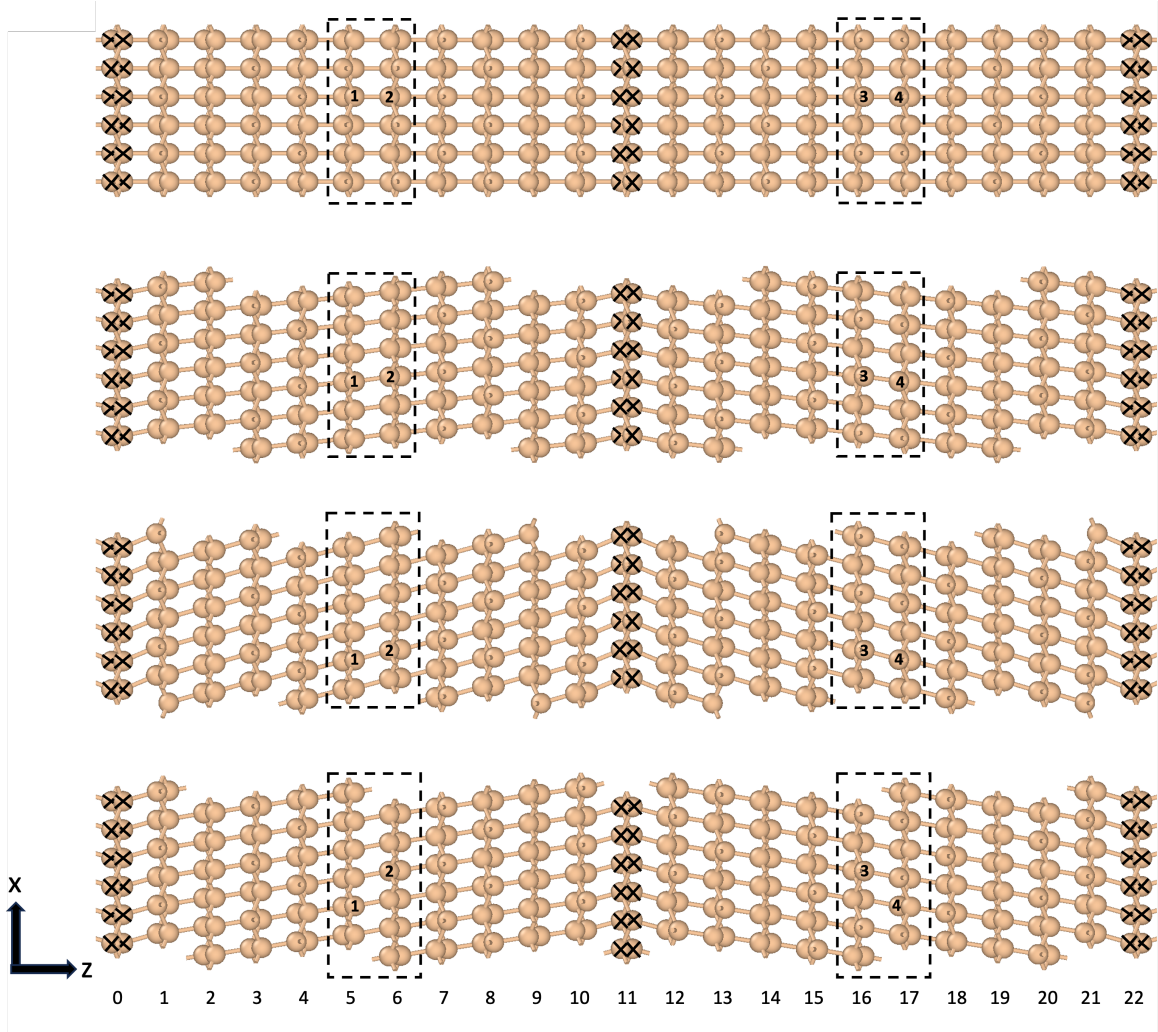
Figure 3: Snapshots along the GB sliding simulations for the $\Sigma 3$ {111} GB with 11 silicon layers between the GBs. The cell has been tripled in the x direction (with respect to the cell used in the calculation) for clarity. Snapshots from top to bottom are at relative displacements of 0, 3.865, 8.506 and 9.279 Å respectively. The dashed boxes indicate GBs, numbers at the bottom indicate layer index and numbers on the atoms indicate the relative movement between grain boundary layers. Layers 0, 11 and 22 are kept fixed (indicated by cross marks), while layer 11 is displaced. Sliding at the GB occurs in the bottom snapshot.
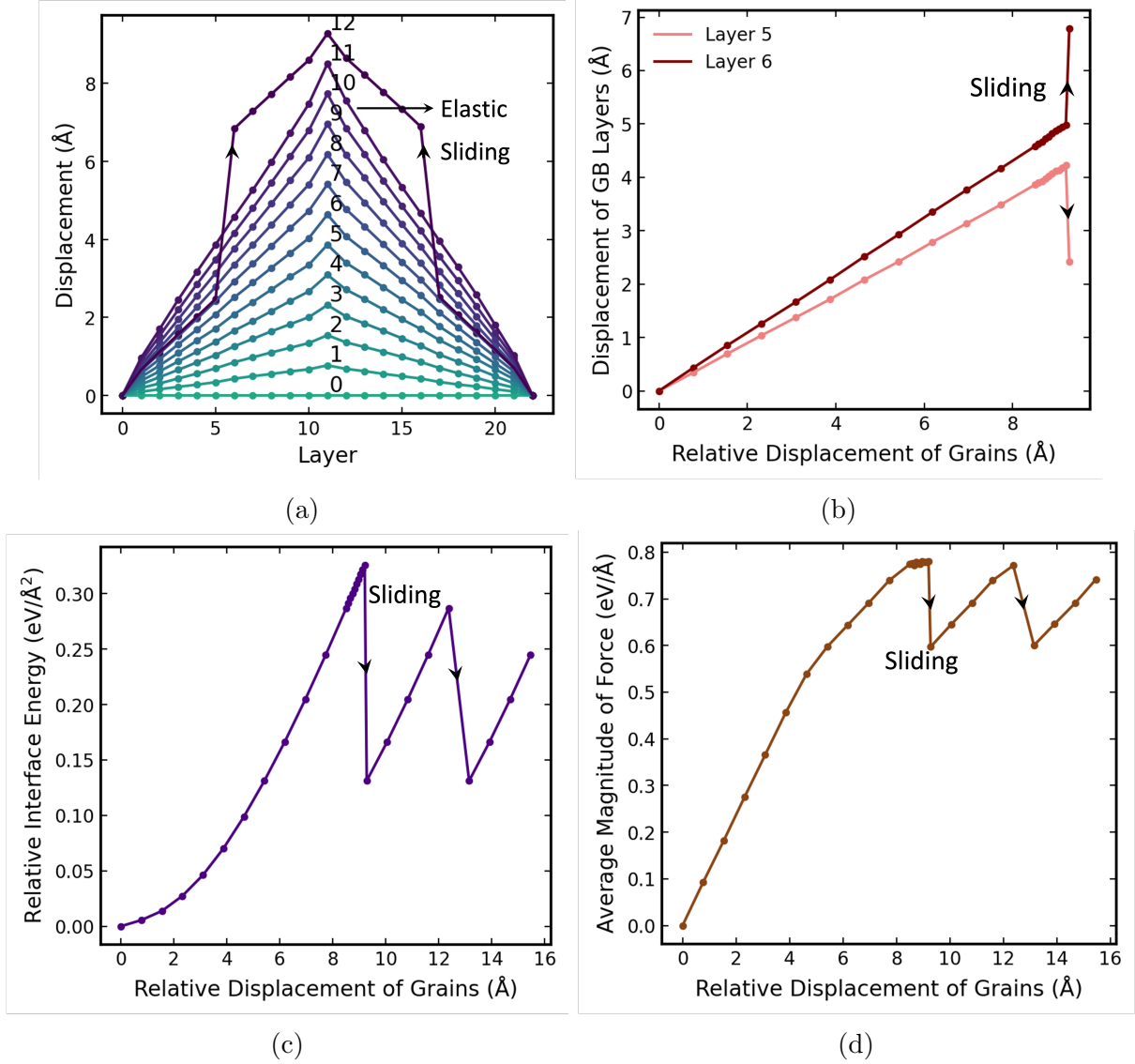
Figure 4: GB sliding simulations for the $\Sigma 3$ {111} GB with 11 silicon layers between the GBs. (a) Displacement as a function of the layer index with increasing relative displacement between grains. Layers 0, 11 and 22 are kept fixed, while the layer 11 is displaced (See Figure 1 for the structure). The step number is indicated on each line where each step corresponds to a relative displacement of 0.773 Å; (b) Displacement of the 5th and 6th layers (GB layers) with increasing relative displacement between the grains including the ten simulations with a finer displacement of 0.077 Å between the relative displacement of 8.506 Å and 9.279 Å; (c) Relative interface energy (the difference between interface energy and interface energy of undeformed GB) versus the relative displacement between the grains including the ten simulations with a finer displacement of 0.077 Å between the relative displacement of 8.506 Å and 9.279 Å; and (d) Average magnitude of force experienced by the atoms that are fixed in layer 0, 11 and 22 (refer to Figure 1 and 3) as a function of relative displacement of the grains including the ten simulations with a finer displacement of 0.077 Å between the relative displacement of 8.506 Å and 9.279 Å.

Effect of Aluminum on GB Sliding

In order to check our hypothesis, firstly, we used basin hopping as described in Section II to understand the segregation of aluminum in the grain boundary, for up to 4 aluminum per GB. We are not considering the presence of oxygen in the system owing to its removal due to the reducing potential in the first battery cycle. Aluminum is allowed to substitute in place of GB silicon atoms. The number of aluminum substituted and their positions are chosen randomly in each step. Each basin hopping is run for 100 steps. The results of basin hopping for the 4 aluminum per GB case are represented in the Supporting Information Figure S6 and S7. From Figure S2a, we can observe that higher energy states are attained throughout the run, switching from one to the other, enabling a wide exploration window. Moreover, a broad range of energies (0.7 eV - 1.1 eV) are covered in the run as can be seen in Figure S2b. The resulting global minimum has a characteristic feature, i.e., all the aluminum atoms are in a single layer. This is a consequence of the phase diagram of silicon-aluminum, where aluminum has very low solubility in silicon, and therefore aluminum atoms prefer to accumulate together.

After identifying the optimal aluminum segregation configurations for different numbers of aluminum, our subsequent step involved conducting GB sliding simulations using these configurations. Each simulation consisted of 20 steps, with each step corresponding to a relative displacement of 0.773 Å, similar to the one used for pure Si GB. The results from GB sliding simulations for the scenario with four aluminum atoms per GB are presented in Figure 5. The results for one, two and three aluminum atoms per GB are available in the Supporting Information (Figure S8, S9 and S10). Several significant differences between GB sliding with and without aluminum are discernible: (a) The sliding barrier is remarkably lowered to 0.0385 eV/Å², representing about 12% of the case without aluminum as can be seen in Figure 5c. Moreover, this value is merely 40% of the interface energy of the undeformed GB with aluminum. (b) The peak force of the system with aluminum has dropped by 66 % in comparison to the system without aluminum as shown in Figure 5d. This reduction

suggests that the presence of aluminum mitigates the rigidity of the GB, enabling sliding, contributing to effective stress relief, and, ultimately, preventing mechanical failure; (c) In contrast to sliding without aluminum, the frequency of sliding is notably higher. Sliding occurred at a relative displacement of 3.634 Å, compared to a relative displacement of 9.279 Å in the absence of aluminum, as depicted in Figure 5b. This increased sliding frequency plays a crucial role in averting the accumulation of excessive stress in the material and (d) Following each sliding event, the GB rapidly returned to its completely undeformed state. This observation indicates substantial stress alleviation due to the presence of aluminum. These findings collectively validate our hypothesis that aluminum facilitates GB sliding, thereby reducing the likelihood of mechanical failure within the material.
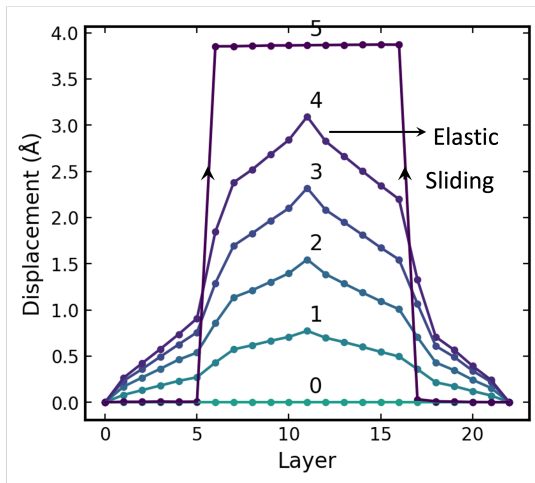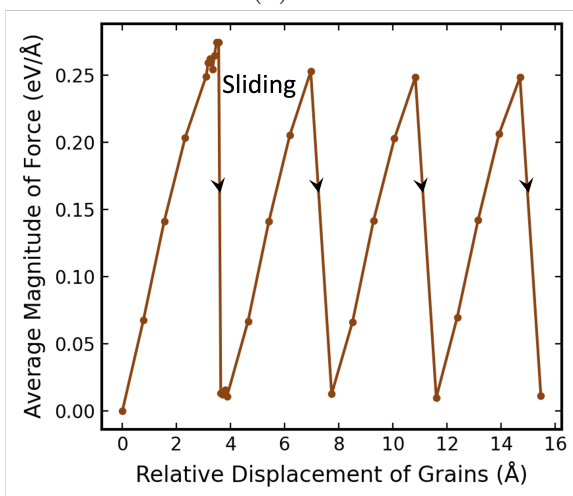

(a)
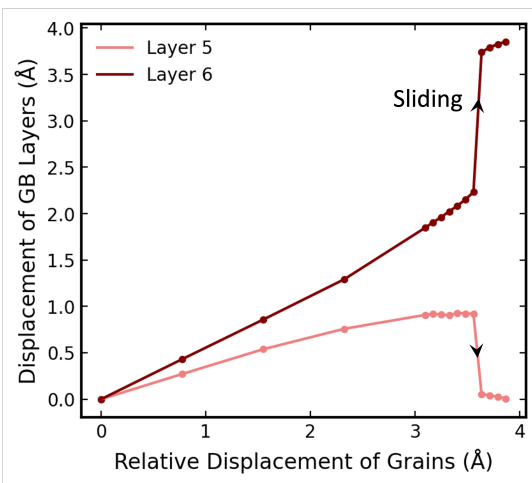
(b)
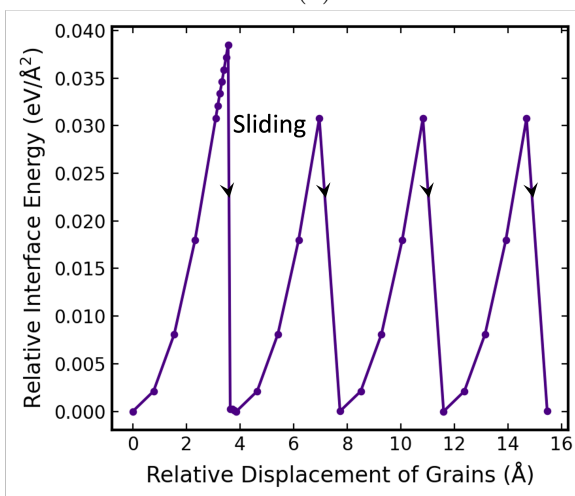
(c)

(d)

Figure 5: GB sliding simulations for the $\Sigma 3$ {111} GB with 11 silicon layers between the GBs and 4 Al per GB. (a) Displacement as a function of the layer index with increasing relative displacement between grains. Layers 0, 11 and 22 are kept fixed, while the layer 11 is displaced (See Figure 1 and 3 for the structure). The step number is indicated on each line where each step corresponds to a relative displacement of 0.773 Å; (b) Displacement of the 5th and 6th layers (GB layers) with increasing relative displacement between the grains; (c) Relative interface energy (the difference between interface energy and interface energy of undeformed GB) versus the relative displacement between the grains including the ten simulations with a finer displacement of 0.077 Å between the relative displacement of 3.093 Å and 3.866 Å, and (d) Average magnitude of force experienced by the atoms that are fixed in layer 0, 11 and 22 (refer Figure 1) as a function of relative displacement of the grains including the ten simulations with a finer displacement of 0.077 Å between the relative displacement of 3.093 Å and 3.866 Å.

The observed outcomes are contingent on the aluminum content per grain boundary (GB). However, the influence of the number of aluminum atoms at the GB on the sliding behavior exhibits a nuanced pattern, graphically represented in Figure 6. The introduction of one aluminum per GB yields a substantial 49% reduction in the sliding barrier. The introduction of second and third aluminum per GB further decreases the barrier by 18% and 21% respectively. However, when the aluminum content increases from 3 to 4 atoms per GB, the sliding barrier is more or less stable, and diminishes with a mere decrease of 0.3%. This suggests that beyond a certain threshold, additional aluminum content has only a minor impact on GB sliding. Another crucial factor to consider is the concurrent increase in interface energy with rising aluminum content. This counters the reduction in the sliding barrier attributed to aluminum's presence by making the initial interface formation more challenging. Therefore, selecting the optimal aluminum content in the silicon anode entails a delicate balance between reducing the sliding barrier and managing the associated increase in interface energy.
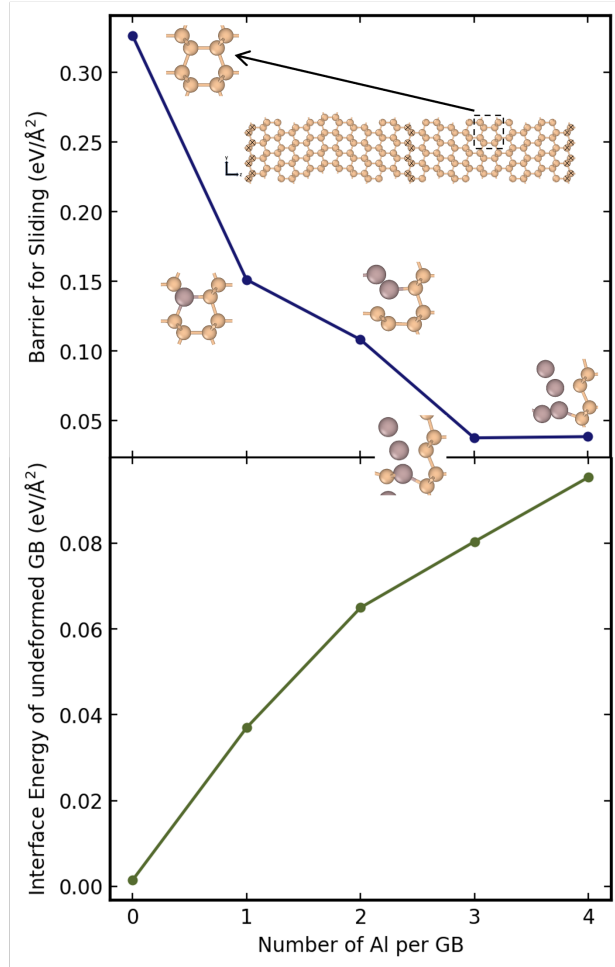
Figure 6: Effect of aluminum content on GB sliding barrier and interface energy. The grey spheres indicate aluminum and the yellow spheres indicate silicon. Top: Barrier for sliding versus the number of aluminum per GB and Bottom: Interface energy of undeformed GB versus the number of aluminum per GB.

Effect of Number of Layers on GB Sliding

To understand the effect of the number of layers in the GB model, we performed simulations with values ranging from 7 to 13 layers per grain for systems with and without aluminum. The results are graphically represented in Figure 7a. Our analysis revealed that the maximum force required to initiate GB sliding remained consistent across all the structures with the same number of aluminum per GB. This observation implies that the number of layers within the GB has no discernible impact on the sliding behavior. However, there are interesting

differences between the structures with and without aluminum as represented in Figure 7. First, the maximum displacement of grains before sliding increases with the number of layers and is hence not an intrinsic parameter describing the sliding. This is because a specific displacement per layer is required to induce the shear (or force) for GB sliding. Furthermore, from Figure 7c, the reduction in slope indicates that the maximum relative displacement of grains before the sliding event occurred became a weaker function of the number of layers when aluminum is added to the system. A notable observation for systems with aluminum is, that even though there is an increasing amount of rigid Si-Si bonds as the number of layers per GB increases, this has no significant impact on the sliding indicating that the aluminum at the GB plays a major role in facilitating sliding. In the presence of Al at the GB, a displacement between grains results in an equivalent shear at the GB interface because this is the weakest part. In the case of pure silicon, the deformation is distributed within the grain and at the GB interface.

(a) No Al

(b) 4 Al per GB
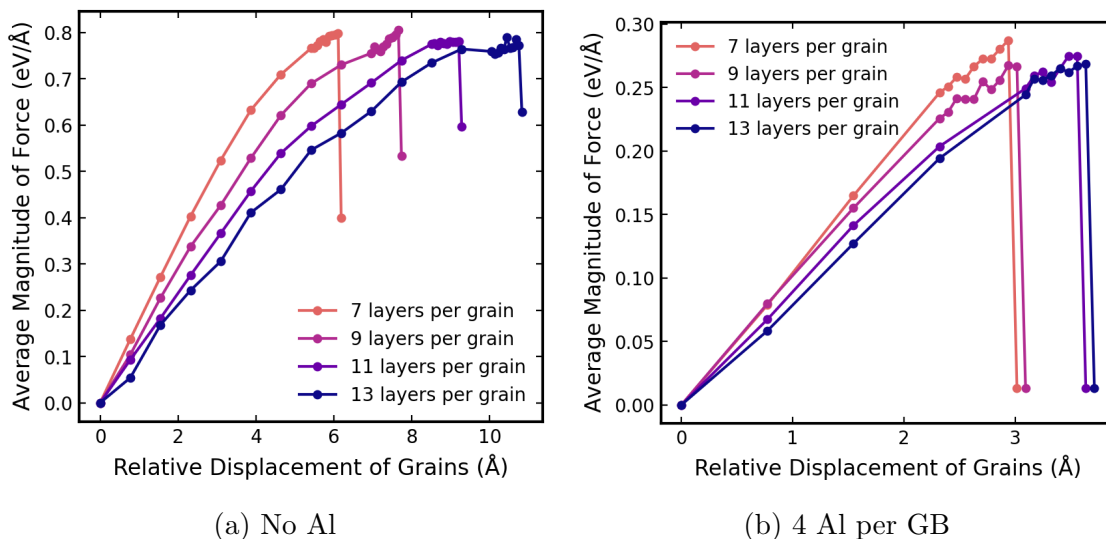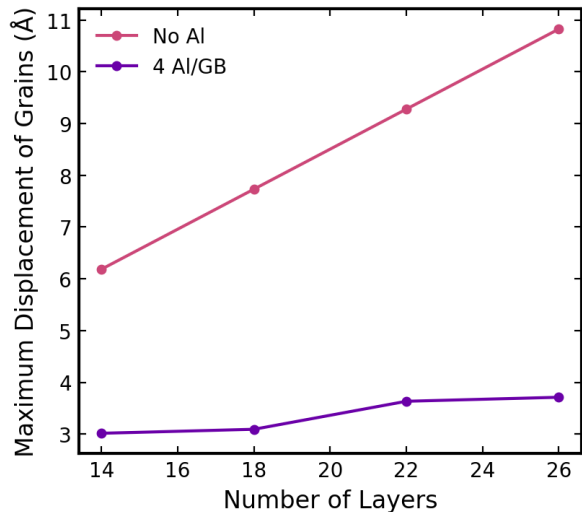
(c)

Figure 7: The effect of the number of layers on GB sliding. (a) The average magnitude of force experienced by the atoms that are fixed versus the relative displacement of grains for different layered GB structures, (b) The average magnitude of force experienced by the atoms that are fixed versus the relative displacement of grains for different layered GB structures with 4 Al per GB, and (c) The maximum relative displacement of grains as a function of number of layers in the GB for systems without and with aluminum.

Understanding Bonding in the GB using COHP

To delve into the underlying chemical mechanisms governing the impact of aluminum on grain boundary (GB) sliding, we utilized Crystal Orbital Hamilton Population (COHP) analysis, facilitated by the Local-Orbital Basis Suite Towards Electronic Structure Reconstruction (LOBSTER) code.[52] This analytical approach provides insights into the atomic bonding interactions within a given structure, with particular emphasis on the quantification of bond strength through Integrated COHP (ICOHP) values. A higher ICOHP value signifies a stronger bond. In the absence of aluminum, the sole bonds present in the GB are Si-Si bonds, which exhibit an ICOHP value of 4.380. However, when aluminum is introduced at the GB, the landscape shifts. Some Si-Si bonds are supplanted by Al-Si bonds, characterized by an ICOHP value of 3.774, indicative of weaker binding. Furthermore, the bonding states for Si-Si are comparatively higher than the bonding states of Al-Si (refer the green area in

Figure 8). This contrast highlights the weaker nature of Al-Si bonds in comparison to their Si-Si counterparts. Consequently, this disparity in bond strength facilitates more facile bond reconstructions during GB sliding, a phenomenon akin to a lubricating effect induced from the presence of aluminum.
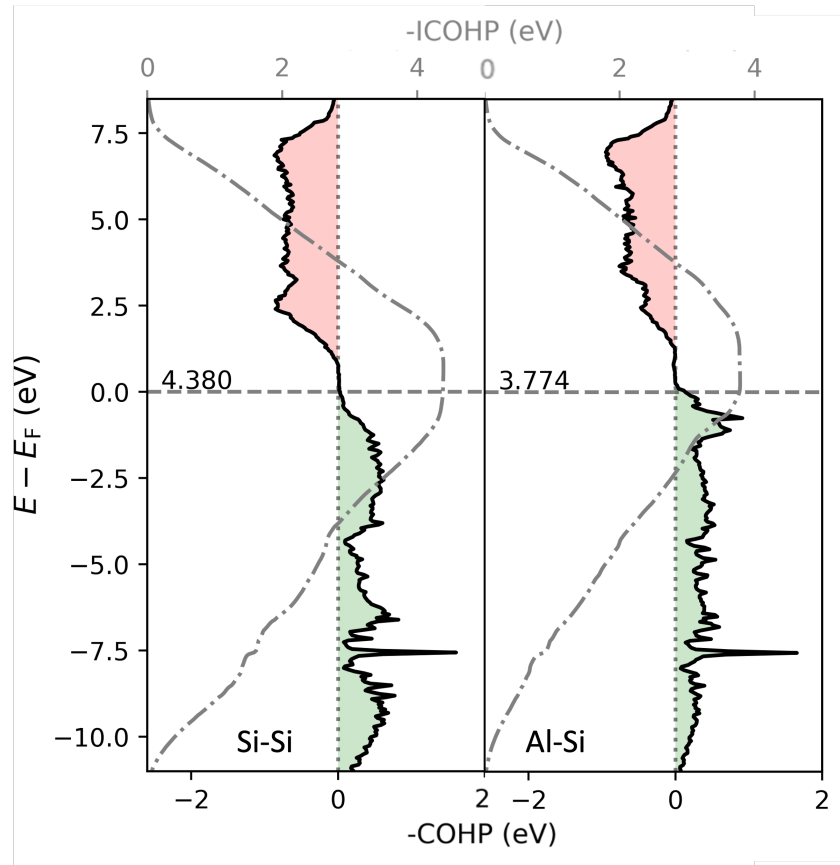

Figure 8: COHP (solid line) and ICOHP (dash-dot line) curves versus one-electron energy (using the traditional x(y) representation). Left: Si-Si bonds at the GB for the pure Si case and Right: Al-Si bonds. The green area signifies bonding states and the red area signifies anti-bonding states. Only bonding states are populated.
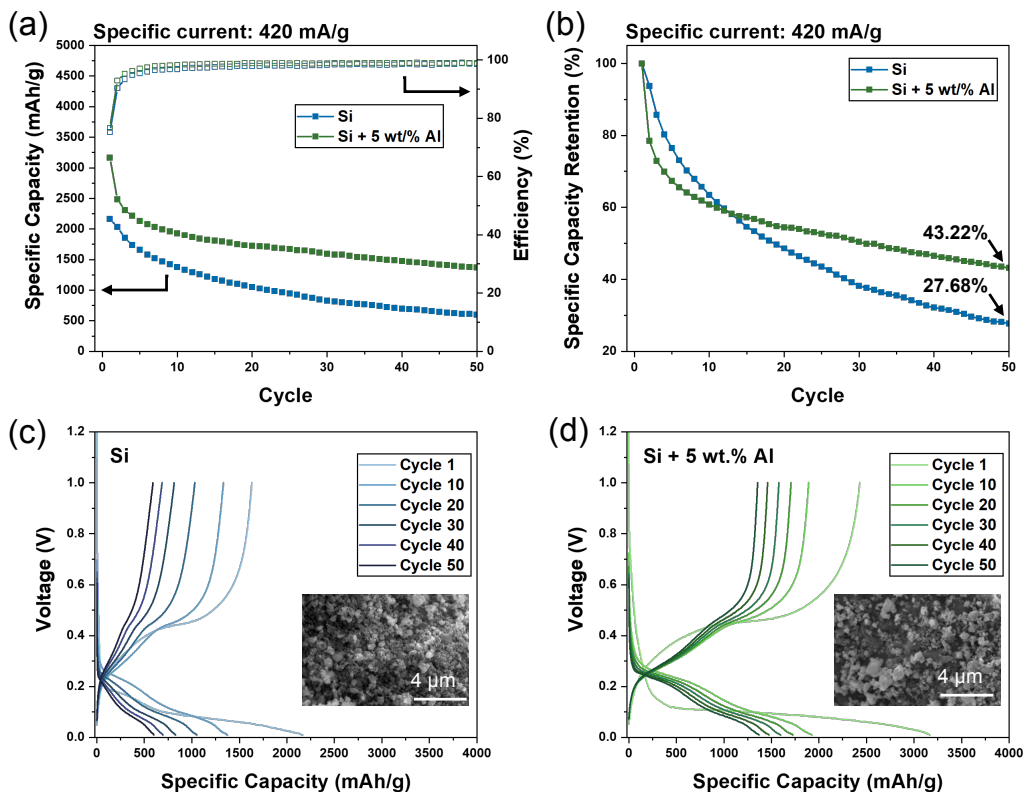
Improvements of Capacity Retention

Figure 9: The cycling stability test of pristine high-energy-ball-milled Si and Si with 5 wt.% Al dopant. (a) Specific discharge capacity (left) with coulombic efficiency profiles (right) and (b) normalized capacity retention of pristine ball-milled Si (blue) and Si with 5 wt.% Al (green) at 0.1C. The charge/discharge voltage profiles of (c) pristine ball-milled Si and (d) Si + 5 wt.% Al with insets of secondary electron images of as-milled powders.

The prepared Al-doped Si anode exhibits enhanced capacity retention up to 43.22% at 50 cycles in the cycling stability test at 0.1 C, which outperforms the retention percentage of pristine Si anode (27.68%), shown in Figure 9a and 9b. The coulombic efficiency of Al-doped Si anode reaches 97.02% at the 5th cycle (versus 95.51% of pristine Si), which indicates improved reversibility of the chemical reactions. The morphology and primary particle size of the Al-doped and undoped Si samples are similar as observed from SEM images in Figures 9c and 9d insets. However, the Al-doped Si shows a higher initial specific discharged capacity of 3166.9 mAh/g compared to pristine Si and also less decay within the first 30 cycles, as shown in Figures 9c and 9d. The cycling testing results validate the simulation we present

22

in this work on improving the structural integrity and mechanical properties of Si anodes through GB sliding induced by Al, which further retains cycling performance.

Conclusion

This study presents a combined theoretical and experimental investigation into the impact of trace aluminum doping on grain boundary sliding, an important phenomenon dictating the mechanical stability in silicon electrodes for Li-ion batteries. We developed and validated a grain boundary sliding model using density functional theory (DFT), demonstrating its consistency with previous findings. Basin hopping, a global optimization technique, is used to identify the most favorable aluminum segregation configuration. Subsequent sliding simulations revealed facilitation of GB sliding and prevention of stress build up in doped compared to undoped silicon. Notably, a strong dependence on aluminum concentration was observed at lower concentrations and diminishing dependence at higher concentrations, confirming the effectiveness of trace doping. COHP analysis revealed weaker Si-Al bonds compared to Si-Si bonds as the mechanism behind improved sliding and reduced stress accumulation. Experimental capacity retention tests on a 5 wt.% Al-doped silicon sample corroborated our theoretical predictions, showing significantly enhanced cyclic stability and material decay reduction. These findings highlight the potential of trace aluminum doping to improve Li-ion battery performance. Moving beyond aluminum, this theoretical framework opens avenues for exploring a vast variety of potential doping materials, fostering the development of next-generation Li-ion batteries with vastly improved performance and stability.

Supporting Information

Electron Back-Scattered Diffusion data, Energy-dispersive X-ray spectroscopy, X-ray Photon Spectroscopy, Cell testing, and Transmission Electron Microscopy of the Al-doped Si sample used to perform capacity retention experiments; Basin hopping results for the segregation of

23

aluminum in GB; Effect of aluminum on GB sliding.

Conflicts of Interest

There are no conflicts to declare.

Acknowledgements

References

(1) Kim, M. G.; Cho, J. Reversible and high-capacity nanostructured electrode materials for Li-ion batteries. *Advanced Functional Materials* **2009**, *19*, 1497–1514.

(2) Boukamp, B.; Lesh, G.; Huggins, R. All-solid lithium electrodes with mixed-conductor matrix. *Journal of the Electrochemical Society* **1981**, *128*, 725.

(3) Shukla, A.; Prem Kumar, T. Materials for next-generation lithium batteries. *Current science* **2008**, *94*, 314–331.

(4) Beaulieu, L.; Eberman, K.; Turner, R.; Krause, L.; Dahn, J. Colossal reversible volume changes in lithium alloys. *Electrochemical and Solid-State Letters* **2001**, *4*, A137.

(5) Kasavajjula, U.; Wang, C.; Appleby, A. J. Nano-and bulk-silicon-based insertion anodes for lithium-ion secondary cells. *Journal of power sources* **2007**, *163*, 1003–1039.

(6) Wu, H.; Cui, Y. Designing nanostructured Si anodes for high energy lithium ion batteries. *Nano today* **2012**, *7*, 414–429.

(7) Ryu, J. H.; Kim, J. W.; Sung, Y.-E.; Oh, S. M. Failure modes of silicon powder negative electrode in lithium secondary batteries. *Electrochemical and solid-state letters* **2004**, *7*, A306.

(8) Rahman, M. A.; Song, G.; Bhatt, A. I.; Wong, Y. C.; Wen, C. Nanostructured silicon anodes for high-performance lithium-ion batteries. *Advanced Functional Materials* **2016**, *26*, 647–678.

(9) Huggins, R. A. Lithium alloy negative electrodes. *Journal of Power Sources* **1999**, *81*, 13–19.

(10) McDowell, M. T.; Lee, S. W.; Wang, C.; Cui, Y. The effect of metallic coatings and crystallinity on the volume expansion of silicon during electrochemical lithiation/delithiation. *Nano Energy* **2012**, *1*, 401–410.

(11) Zuo, X.; Zhu, J.; Müller-Buschbaum, P.; Cheng, Y.-J. Silicon based lithium-ion battery anodes: A chronicle perspective review. *Nano Energy* **2017**, *31*, 113–143.

(12) Magasinski, A.; Dixon, P.; Hertzberg, B.; Kvit, A.; Ayala, J.; Yushin, G. High-performance lithium-ion anodes using a hierarchical bottom-up approach. *Nature materials* **2010**, *9*, 353–358.

(13) Kim, W.-S.; Hwa, Y.; Shin, J.-H.; Yang, M.; Sohn, H.-J.; Hong, S.-H. Scalable synthesis of silicon nanosheets from sand as an anode for Li-ion batteries. *Nanoscale* **2014**, *6*, 4297–4302.

(14) Jung, H.; Kim, Y.-U.; Sung, M.-S.; Hwa, Y.; Jeong, G.; Kim, G.-B.; Sohn, H.-J. Nanosize Si anode embedded in super-elastic nitinol (Ni–Ti) shape memory alloy matrix for Li rechargeable batteries. *Journal of Materials Chemistry* **2011**, *21*, 11213–11216.

(15) Hwang, C.-M.; Lim, C.-H.; Yang, J.-H.; Park, J.-W. Electrochemical properties of negative SiMox electrodes deposited on a roughened substrate for rechargeable lithium batteries. *Journal of Power Sources* **2009**, *194*, 1061–1067.

(16) Li, T.; Cao, Y.; Ai, X.; Yang, H. Cycleable graphite/FeSi6 alloy composite as a high capacity anode material for Li-ion batteries. *Journal of Power Sources* **2008**, *184*, 473–476.

(17) Chen, Y.; Qian, J.; Cao, Y.; Yang, H.; Ai, X. Green synthesis and stable Li-storage performance of FeSi2/Si@ C nanocomposite for lithium-ion batteries. *ACS applied materials & interfaces* **2012**, *4*, 3753–3758.

(18) Yan, J.; Huang, H.; Zhang, J.; Yang, Y. The study of Mg2Si/carbon composites as anode materials for lithium ion batteries. *Journal of power sources* **2008**, *175*, 547–552.

(19) Zhang, R.; Du, Y.; Li, D.; Shen, D.; Yang, J.; Guo, Z.; Liu, H. K.; Elzatahry, A. A.; Zhao, D. Highly reversible and large lithium storage in mesoporous Si/C nanocomposite anodes with silicon nanoparticles embedded in a carbon framework. *Advanced Materials* **2014**, *26*, 6749–6755.

(20) Hwa, Y.; Kim, W.-S.; Hong, S.-H.; Sohn, H.-J. High capacity and rate capability of core–shell structured nano-Si/C anode for Li-ion batteries. *Electrochimica Acta* **2012**, *71*, 201–205.

(21) Liu, N.; Wu, H.; McDowell, M. T.; Yao, Y.; Wang, C.; Cui, Y. A yolk-shell design for stabilized and scalable Li-ion battery alloy anodes. *Nano letters* **2012**, *12*, 3315–3321.

(22) Liu, P.; Zheng, J.; Qiao, Y.; Li, H.; Wang, J.; Wu, M. Fabrication and characterization of porous Si-Al films anode with different macroporous substrates for lithium-ion batteries. *Journal of Solid State Electrochemistry* **2014**, *18*, 1799–1806.

(23) He, Y.; Yu, X.; Wang, Y.; Li, H.; Huang, X. Alumina-coated patterned amorphous silicon as the anode for a lithium-ion battery with high Coulombic efficiency. *Advanced materials* **2011**, *23*, 4938–4941.

(24) Tesfaye, A. T.; Gonzalez, R.; Coffer, J. L.; Djenizian, T. Porous silicon nanotube arrays as anode material for Li-ion batteries. *ACS applied materials & interfaces* **2015**, *7*, 20495–20498.

(25) Cho, J. Porous Si anode materials for lithium rechargeable batteries. *Journal of Materials Chemistry* **2010**, *20*, 4009–4014.

(26) Meyers, M. A.; Mishra, A.; Benson, D. J. Mechanical properties of nanocrystalline materials. *Progress in materials science* **2006**, *51*, 427–556.

(27) Ashby, M. Boundary defects, and atomistic aspects of boundary sliding and diffusional creep. *Surface Science* **1972**, *31*, 498–542.

(28) Weinberg, F. Grain boundary shear in aluminum. *Acta Metallurgica* **1954**, *2*, 889–890.

(29) Bell, R.; Langdon, T. An investigation of grain-boundary sliding during creep. *Journal of Materials Science* **1967**, *2*, 313–323.

(30) Adsit, N.; Brittain, J. GRAIN BOUNDARY SLIDING VERSUS GRAIN BOUNDARY MIGRATION IN CREEP. 1960.

(31) Puttick, K.; King, R. Boundary Slip in Bicrystals of Tin. *Journal of the Institute of Metals* **1952**, *80*, 537.

(32) Intrater, J.; Machlin, E. A method for growing bicrystals of copper. *AIME TRANS* **1959**, *215*, 471–472.

(33) Maji, R.; Luppi, E.; Capron, N.; Degoli, E. Ab initio study of oxygen segregation in silicon grain boundaries: The role of strain and vacancies. *Acta Materialia* **2021**, *204*, 116477.

(34) Käshammer, P.; Sinno, T. Interactions of twin boundaries with intrinsic point defects and carbon in silicon. *Journal of Applied Physics* **2013**, *114*, 083505.

(35) Chen, J.; Sekiguchi, T. Carrier Recombination Activity and Structural Properties of Small-Angle Grain Boundaries in Multicrystalline Silicon. *Japanese Journal of Applied Physics* **2007**, *46*, 6489, Publisher: IOP Publishing.

(36) Kresse, G.; Hafner, J. Ab initio molecular dynamics for liquid metals. *Physical review B* **1993**, *47*, 558.

(37) Larsen, A. H.; Mortensen, J. J.; Blomqvist, J.; Castelli, I. E.; Christensen, R.; Dułak, M.; Friis, J.; Groves, M. N.; Hammer, B.; Hargus, C.; others The atomic simulation environment—a Python library for working with atoms. *Journal of Physics: Condensed Matter* **2017**, *29*, 273002.

(38) Bhimineni, S. H.; Xia, Y. Scalar Codes. `https://github.com/sreeharshab/scalar_codes`.

(39) Perdew, J. P.; Burke, K.; Ernzerhof, M. Generalized gradient approximation made simple. *Physical review letters* **1996**, *77*, 3865.

(40) Monkhorst, H. J.; Pack, J. D. Special points for Brillouin-zone integrations. *Physical review B* **1976**, *13*, 5188.

(41) Wales, D. J.; Doye, J. P. Global optimization by basin-hopping and the lowest energy structures of Lennard-Jones clusters containing up to 110 atoms. *The Journal of Physical Chemistry A* **1997**, *101*, 5111–5116.

(42) Metropolis, N.; Ulam, S. The monte carlo method. *Journal of the American statistical association* **1949**, *44*, 335–341.

(43) Sun, G.; Alexandrova, A. N.; Sautet, P. Pt8 cluster on alumina under a pressure of hydrogen: Support-dependent reconstruction from first-principles global optimization. *The Journal of chemical physics* **2019**, *151*.

(44) Okada, Y.; Tokumaru, Y. Precise determination of lattice parameter and thermal expansion coefficient of silicon between 300 and 1500 K. *Journal of applied physics* **1984**, *56*, 314–320.

(45) Ratanaphan, S.; Yoon, Y.; Rohrer, G. S. The five parameter grain boundary character distribution of polycrystalline silicon. *Journal of materials science* **2014**, *49*, 4938–4945.

(46) Murray, J.; McAlister, A. The Al-Si (aluminum-silicon) system. *Bulletin of alloy phase diagrams* **1984**, *5*, 74–84.

(47) Chen, G.-H. Mechanical activation of calcium aluminate formation from CaCO3–Al2O3 mixtures. *Journal of alloys and compounds* **2006**, *416*, 279–283.

(48) McDowell, M. T.; Lee, S. W.; Nix, W. D.; Cui, Y. 25th Anniversary Article: Understanding the Lithiation of Silicon and Other Alloying Anodes for Lithium-Ion Batteries. *Advanced Materials* **2013**, *25*, 4966–4985.

(49) Rahaman, O.; Mortazavi, B.; Rabczuk, T. A first-principles study on the effect of oxygen content on the structural and electronic properties of silicon suboxide as anode material for lithium ion batteries. *Journal of Power Sources* **2016**, *307*, 657–664.

(50) Ivanov, V.; Mishin, Y. Dynamics of grain boundary motion coupled to shear deformation: An analytical model and its verification by molecular dynamics. *Physical Review B* **2008**, *78*, 064106.

(51) Wan, L.; Wang, S. Shear response of the $\Sigma 9 \langle 110 \rangle \{221\}$ symmetric tilt grain boundary in fcc metals studied by atomistic simulation methods. *Physical Review B* **2010**, *82*, 214112.

(52) Maintz, S.; Deringer, V. L.; Tchougréeff, A. L.; Dronskowski, R. LOBSTER: A tool to extract chemical bonding from plane-wave based DFT. 2016.